

REPORT DOCUMENTATION PAGE**Form Approved**
OMB No. 0704-0188

Public reporting burden for this collection of information is estimated to average 1 hour per response, including the time for reviewing instructions, searching data sources, gathering and maintaining the data needed, and completing and reviewing the collection of information. Send comments regarding this burden estimate or any other aspect of this collection of information, including suggestions for reducing this burden to Washington Headquarters Service, Directorate for Information Operations and Reports, 1215 Jefferson Davis Highway, Suite 1204, Arlington, VA 22202-4302, and to the Office of Management and Budget, Paperwork Reduction Project (0704-0188) Washington, DC 20503.

PLEASE DO NOT RETURN YOUR FORM TO THE ABOVE ADDRESS.

1. REPORT DATE (DD-MM-YYYY)		2. REPORT TYPE Final Technical Report		3. DATES COVERED (From - To) 01 March 2004 – 28 February 2007	
4. TITLE AND SUBTITLE Ultra High Pressure Air Properties and CFD Code				5a. CONTRACT NUMBER FA9550-04-1-0089	
				5b. GRANT NUMBER	
				5c. PROGRAM ELEMENT NUMBER	
6. AUTHOR(S) Professor Charles L. Merkle				5d. PROJECT NUMBER	
				5e. TASK NUMBER	
				5f. WORK UNIT NUMBER	
7. PERFORMING ORGANIZATION NAME(S) AND ADDRESS(ES) Schools of Astronautics and Aeronautical Engineering & Mechanical Engineering Purdue University West Lafayette				8. PERFORMING ORGANIZATION REPORT NUMBER	
9. SPONSORING/MONITORING AGENCY NAME(S) AND ADDRESS(ES) Air Force Office of Scientific Research (AFOSR) 875 N. Arlington St., Rm. 3112 Arlington, VA 22203 <i>Dr John Schmissner/NA</i>				10. SPONSOR/MONITOR'S ACRONYM(S) AFOSR	
				11. SPONSORING/MONITORING AGENCY REPORT NUMBER N/A	
12. DISTRIBUTION AVAILABILITY STATEMENT DISTRIBUTION A: Approved for public release; distribution unlimited. AFRL-SR-AR-TR-08-0047					
13. SUPPLEMENTARY NOTES					
14. ABSTRACT The research objectives are to develop effective procedures for computing fluid flow at ultra high pressures where fluids exhibit very different thermodynamic behavior than the perfect gas and incompressible fluid models that are commonly used in CFD simulations. Three issues to be addressed include: developing RANS algorithms for arbitrary fluid applications; developing efficient properties evaluation procedures for arbitrary fluids; and extending hybrid RANS-LES algorithms to high pressures. All three of these issues have been demonstrated.					
15. SUBJECT TERMS					
16. SECURITY CLASSIFICATION OF:		17. LIMITATION OF ABSTRACT	18. NUMBER OF PAGES	19a. NAME OF RESPONSIBLE PERSON	

Final Technical Report

ULTRA HIGH PRESSURE AIR PROPERTIES AND CFD CODE

GRANT FA9550-04-1-0089

Charles L. Merkle

Schools of Astronautics and Aeronautical Engineering and Mechanical Engineering
Purdue University, West Lafayette

Abstract

The research objectives are to develop effective procedures for computing fluid flow at ultra high pressures where fluids exhibit very different thermodynamic behavior than the perfect gas and incompressible fluid models that are commonly used in CFD simulations. Three issues to be addressed include: developing RANS algorithms for arbitrary fluid applications; developing efficient properties evaluation procedures for arbitrary fluids; and extending hybrid RANS-LES algorithms to high pressures. All three of these issues have been demonstrated. A generalized fluid model that is independent of the equation of state has been developed and demonstrated for a wide variety of flows. An adaptive properties evaluation method that is competitive in time with perfect gas calculations but allows highly complex EOS routines like REFPROP, tabular properties data, or simple algebraic relations (such as Peng-Robinson) has been developed. Results for hybrid RANS-LES models that take advantage of the arbitrary scaling used for convergence and accuracy control in the general EOS formulation have also been demonstrated. The hybrid method is efficient at lower cell aspect ratios below 100. Additional work is needed to provide the desired robustness at cell aspect ratios of 1000 and higher. The general equation of state method has been applied to a number of supercritical fluid applications including regenerative heat transfer in a rocket engine chamber and preliminary solutions for combustion problems in which the fuel or oxidizer is supercritical prior to burning. In addition the general equation methodology has been applied to Maxwell's equations to provide a hyperbolic time-marching method that applies in either wave-like Maxwell regimes, or in diffusion-like MHD regimes.

Introduction

Numerous Air Force T&E applications use fluids at ultra high pressures where complex equations of state are required. CFD solutions at these pressures require that the equations be expressed in a form applicable to liquids, vapors and supercritical regions. The numerical algorithm must be applicable over all thermodynamic regimes and across all Mach number ranges. The representative thermodynamics at these conditions are described by advanced EOS techniques such as REFPROP¹ which has currently been updated in a companion effort.² The foundations of the numerical algorithms were developed previously based upon an appropriate scaling of the equations,³ but have been updated in the present work. An efficient properties evaluation procedure has been be

20080131274

devised to ensure effective incorporation in CFD codes. Finally, high Reynolds numbers applications require extensions of LES turbulence techniques to these general fluids.

Equation Formulation

The general equations of motion for multi-component, multi-phase fluids can be expressed in the divergence form, $\nabla \cdot \mathcal{F} = 0$, where ∇ is a four-dimensional space-time operator and $\mathcal{F} = Q\vec{e}_t + E\vec{e}_x + F\vec{e}_y + G\vec{e}_z$. The temporal flux vector includes the density, velocity components, pressure and stagnation enthalpy, $Q = (\rho, \rho u, \rho v, \rho w, \rho h^0 - p)^T$, with similar terms for the spatial fluxes. Numerical solutions do not allow the use of density as an independent variable in thermodynamic ranges where density is essentially constant (liquids), so Q cannot be used as the primary dependent variable. This difficulty can be circumvented by introducing a pseudo-time term, τ , for time-marching and choosing the primitive variables, $Q_p = (p, u, v, w, T)^T$, as the solution variable so that the equation system is expressed as, $\Gamma \partial Q_p / \partial \tau + \nabla \cdot \mathcal{F} = 0$. The pseudo-time coefficient, Γ , provides dimensional consistency and depends on the equation of state through the property derivatives ρ_p , ρ_T , h_p , and h_T which can be obtained from the Gibbs function.² Appropriate scaling of the equations indicates that efficient convergence and uniform solution accuracy over all thermodynamic and Mach number regimes may be achieved by replacing the physical property, ρ_p , by an artificial property, ρ'_p that is based upon the Mach, Reynolds, Strouhal and Froude numbers of the problem.

Properties Evaluation Procedure

Having set the equations of motion and the algorithm, efficient properties evaluation can be obtained by using a Cartesian adaptive table look-up procedure that enables user-defined accuracy over the thermodynamic domain of interest. The Cartesian adaptive method results in a tree structure that provides search procedures in highly non-uniform tables that are competitive with equally spaced tables while also providing the high accuracies in both the thermodynamic functions and their derivatives that are required for CFD calculations. Representative results for CO₂ in Fig. 1 show the grid for a 0.1% accurate solution. The evaluation efficiency of this method in REFPROP tables shows a speed increase between two to three orders of magnitude and CFD computations based on the arbitrary fluid require essentially the same CPU time as those based on a perfect gas.

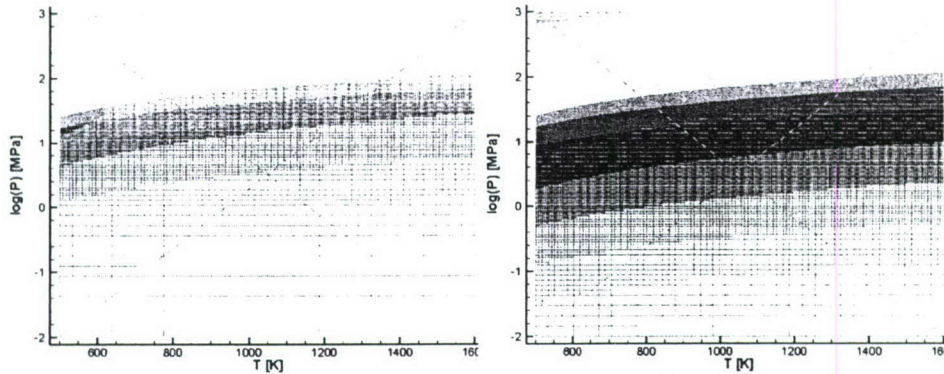


Figure 1. Adaptive interpolation maps for CO_2 . $10^{-2} < p < 10^3 \text{ MPa}$, $500 < T < 1600 \text{ K}$. Left: 1% accuracy, 22,000 points; Right: 0.1% accuracy, 225,000 points.

Three levels of interpolation accuracy have been considered: C^0 , C^1 and C^2 . As is discussed in more detail below, at all three levels of accuracy the final square domains are broken into triangles over which bi-variate interpolation is accomplished. Cell boundaries across which a change in refinement level result in property discontinuities that can adversely impact CFD convergence and accuracy unless care is taken to generate triangles that are consistent with the grid refinement. For the C^0 interpolation, the two thermodynamic functions and their derivatives are all taken as independent linear functions. This implies the derivatives are not consistent with the functions, but ensures derivative continuity across interpolation cell boundaries. The C^1 interpolation uses fifth-order interpolation to give second-order continuity in density and enthalpy at all triangular boundaries. The enthalpy and its derivatives are then evaluated consistently in each triangle and are continuous at cell boundaries. The density and its derivatives are similarly consistent and continuous. The C^2 interpolation uses ninth-order interpolation to give second-order continuity in the Gibbs function so that the enthalpy, density and all four derivatives are mutually consistent and continuous. Results show that all three methods provide effective CFD solutions.

Thermodynamic Consistency and Function Continuity in Properties Reconstruction

For a fluid computation based upon primitive variables, the six thermodynamic properties, ρ , ρ_p , ρ_T , h , h_p , and h_T , and the two transport properties, μ and k , must be evaluated as a function of p and T at every cell and every iteration. There are several potential ways to employ Cartesian adaptive methods to store and recover the data. The most straightforward approach is to store all eight properties at each node of the Cartesian grid and reconstruct all eight properties independently. While this procedure can provide continuous functions across cell boundaries, it produces inconsistent results because it ignores the interdependency of the density and the enthalpy and the four thermodynamic derivatives. To incorporate this characteristic in CFD solutions, the consistency of the property evaluations must be considered.

Thermodynamic consistency in property evaluations has been discussed by Swesty,⁵ who used the Helmholtz free energy as a basis function. His results, which were based on much coarser meshes (and correspondingly lower accuracies) than the ones contemplated here, show that failing to include proper consistency conditions in thermodynamic reconstruction can lead to significant errors in flowfield solutions. Our experience with fine grid interpolation normally keeps the inconsistencies to acceptable levels so that we can use either consistent or inconsistent properties evaluation. Swesty used higher-order reconstruction to maintain second-order consistency throughout a piece-wise continuous domain of quadrilaterals. In analogous fashion, we consider three different levels of reconstruction involving C^0 , C^1 , and C^2 continuity across cell boundaries whose results range from partially to fully consistent. In place of the quadrilateral sub-domains used by Swesty, we reconstruct the property functions over triangles in the mapped domain. With the global structure maintained through the quadrilateral grid, properties are retrieved by first locating the triangle in which their given p and T conditions lie and then using stored values at the vertices to interpolate to the desired degree of accuracy during a numerical simulation.

In the C^0 method, values for all thermodynamic and transport properties are stored at the vertices of each square in the mapped plane. The squares are then subdivided into triangles and the values of each function at the three vertices are used to construct independent bi-linear reconstruction functions for each property. The bi-linear reconstruction used in the C^0 method therefore ensures function continuity along all faces of adjacent cells of the same size for all eight fluid properties but does not provide internal consistency inside the triangles. For example, both density and its first derivatives vary linearly over each triangular region. Further, the enthalpy and density have no interdependence on each other. Nevertheless, by taking the six properties stored at the vertices from a consistent thermodynamic database, the internal inconsistencies remain small on a fine grid.

The alternative of using linear reconstruction over all triangles for the density and enthalpy and differentiating these linear functions to obtain the property derivatives gives improved consistency, but introduces derivative discontinuities at the cell faces. Experience shows that these derivative discontinuities are much more detrimental to CFD solutions than the inconsistencies.

To incorporate property consistency in the reconstructed results we use bivariate polynomials of the form^{22, 23},

$$z(x, y) = \sum_{i=0}^n \sum_{j=0}^{n-i} q_{i,j} x^i y^j \quad (1)$$

to represent the local solution. The number of undetermined constants in a polynomial of degree n is $(n+1)(n+2)/2$. One advantage of the Cartesian subdivision is that these polynomials are especially suitable for triangles. The theory and implementation of polynomials on triangular meshes is well documented (see, for example, Akimo⁶ and Preusser,⁷) and both C^1 and C^2 reconstruction methods based upon the polynomial expansion of Eq. 1 have been considered. The C^1 reconstruction provides consistency between density and its partial derivatives and enthalpy and its partial derivatives, but does not provide consistency between density and enthalpy. We refer to the C^1

reconstruction as partially consistent. The C^2 reconstruction provides fully consistent results. Details of both methods are given below.

The C^1 method treats the density and enthalpy as unrelated functions that are each handled in analogous fashion. Using the density as an example, the goal of C^1 reconstruction is to reconstruct the density function in such a manner that the values of ρ , ρ_n and ρ_τ are consistent within any given cell and that all three quantities are continuous across cell boundaries (*i.e.*, the density is C^1 continuous while the derivatives are C^0 continuous). This level of consistency and continuity can be achieved by using a bi-quintic (fifth-order) polynomial of the form given in Eq. 1. The construction of a bi-quintic polynomial requires the determination of 21 coefficients. Storing the values of the density and its derivatives up to second order at each of the three vertices provides 18 conditions. The remaining three come from the requirement that the derivatives in the direction normal to each edge be continuous. This can be done either by prescribing the normal derivatives or by reducing the order of the polynomials. The later choice is the known as the ‘condensation of parameters’ method.⁶ Since the density and enthalpy are treated independently, the enthalpy and its first two derivatives must also be stored at all vertices. Similar consistency and continuity are then ensured for the enthalpy and its first derivatives. The enthalpy and density are, however, unrelated on a given region so that consistency between these two functions is not guaranteed. Nevertheless, if both density and enthalpy are taken from a database such as REFPROP that is itself consistent, the degree of inconsistency in the C^1 approximation is small.

The C^2 method interpolates all properties and their derivatives by reconstructing the Gibbs function as a ninth-order polynomial which requires the determination of 55 coefficients. Of these, 45 are determined by storing the Gibbs function and its derivatives up to fourth order on the three vertices. Requiring C^2 -continuity on each of the edges provides another nine conditions. The final condition can be specified at will without violating the smoothness constraints, while still keeping the fit to the nodal data. Additional details of the formulation are given in the literature.⁶ In the C^2 method, only the Gibbs function is reconstructed and all six thermodynamic properties are computed from this single function resulting in properties that are fully consistent with each other and the underlying Gibbs function. All six thermodynamic properties are based upon higher order variations of the Gibbs function across each triangle with first- and second-derivative continuity across all adjoining faces. This results in consistency and continuity among all six properties. The resulting density and enthalpy reconstructions are consistent and C^1 continuous, while their derivatives are consistent and C^0 continuous.

For all three reconstruction levels, the coefficients of the piecewise function are stored for each triangle once they have been calculated and need not be updated in CFD calculations. In the following section we discuss appropriate triangulation methods for effectively implementing the C^0 , C^1 , and C^2 methods on the adaptive Cartesian grid.

Triangulation on Unequally Sized Squares. In equally spaced regions of a Cartesian mesh where all neighbors are the same size, the squares can be split into triangles by dividing along either diagonal and any of the three reconstruction methods described above can be applied on the resulting triangles. The situation is somewhat more complex when two neighboring cells are unequal. For example, the line l shown in Fig. 2 which crosses face AF between cells of two different refinement levels. The simple diagonal

triangulation indicated in Fig. 2 results in a property discontinuity at this interface for either the C^0 , C^1 or C^2 reconstruction procedures because the properties on the left side of the interface (point, P_L) are determined by values of the function at vertices A and F, while those on the right side (point P_R) are determined by vertices A and D.

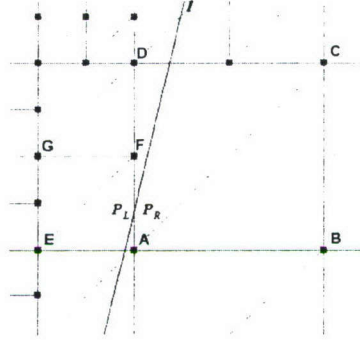


Figure 2. Details of diagonal triangulation on a square mesh at a change in cell size.

This difficulty is demonstrated in Fig. 3 which compares the reconstructions along line I of the density (left) and its pressure derivative, ρ_p (right), based upon the triangulation shown in Fig. 2 with the exact solution as functions of temperature. In addition, the reconstruction based upon an alternative triangulation discussed below is also presented. The discontinuity at the interface for the simple diagonal triangulation (Fig. 4) is readily visible. The reconstructions in Fig. 3 were obtained by using the C^0 method, but reconstructions based on C^1 or C^2 exhibit similar discontinuities. Further, the discontinuity exists regardless of which diagonal is used to bisect the squares.

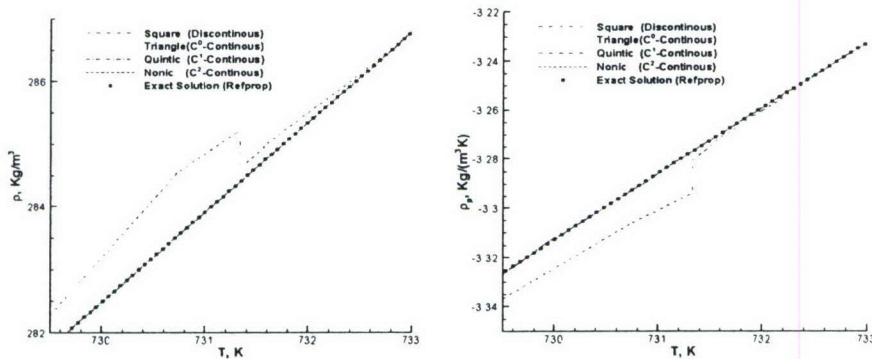


Figure 3. Reconstructed values of ρ and ρ_p for triangulations in Fig. 2 (Long dashed line) and Fig. 6 (short-dashed and dotted lines) along line I in Figs. 2 and 6. Exact solution given by dotted points.

To demonstrate the impact that discontinuities of this nature have on CFD calculations, we show the results of one-dimensional CFD solution on Fig. 4 and the corresponding convergence plots on Fig. 5. The axial variation of the temperature in Fig. 4 indicates that the discontinuity in properties at a cell size change produces an unphysical wiggle in the solution. The corresponding convergence curve on Fig. 5 also indicates that convergence stalls when it reaches a level consistent with the magnitude of the discontinuity in the reconstructed functions. The remaining convergence curves are discussed below.

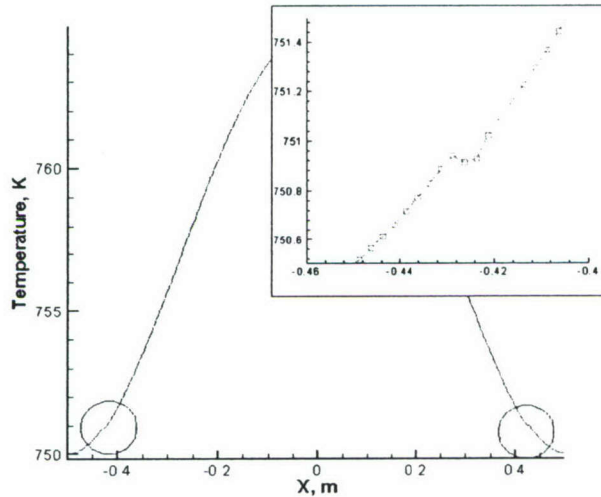


Figure 4. Temperature variation in 1-D computational solution with reconstruction based on diagonally divided squares (Fig. 2) illustrating wiggles created in solution by property discontinuities at cell faces.

Modified Triangulation for Ensuring Continuity. The difficulties arising from unequally sized squares can be rectified by triangulating the Cartesian mesh in a manner that ensures the reconstructions on both sides of the interface are based on the same data. One acceptable triangulation pattern for a cell with two refined and two unrefined neighbors is demonstrated in Fig. 6. As shown by the subdivision in the figure, the properties on the left and right sides of the boundary at point **P** are each based upon similar values and result in the specified degree of function continuity. The reconstructions of the properties along line **I** across the boundary are now both determined by the values at **A** and **F**. The continuity of the piecewise function across the interface is thus guaranteed as exhibited by the C^0 , C^1 and C^2 reconstruction curves in Fig. 5. The C^0 reconstruction results in a small local error, but this has no adverse impact on the convergence rate (Fig. 7) or the solution (not shown). The reconstructed functions for the C^1 and C^2 reconstruction also provide excellent convergence as Fig. 7 shows. Finally, Fig. 7 shows the convergence rate for a solution for which the properties were taken directly from REFPROP without any reconstruction method. This 'exact' property evaluation method resulted in exactly the same convergence as any of the three

reconstruction levels (although it took much more CPU time). Consequently, we see that a proper triangulation results in both efficient convergence and accurate solutions.

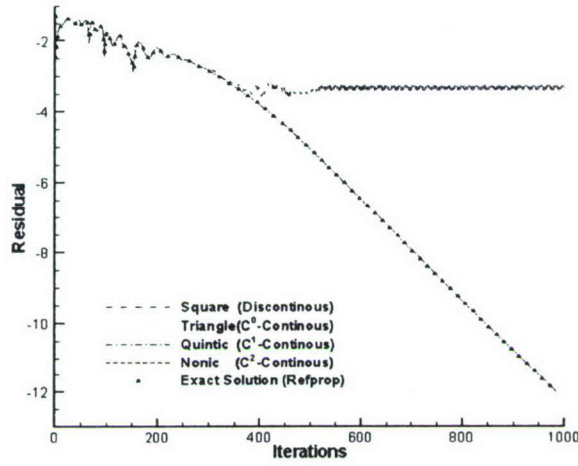


Figure 5. Exemplary plot showing effect of triangulation on convergence of a specific CFD calculation. Red: Triangulation taken from Fig. 4; Green, blue and violet: Triangulation taken from Fig. 6; Triangles: properties evaluated directly from REFPROP.

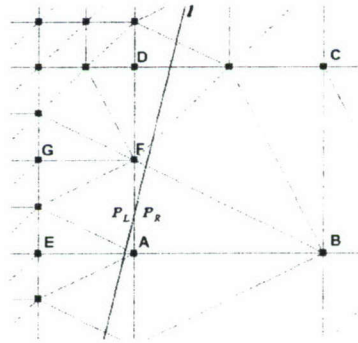


Figure 6. Triangulation method chosen to ensure continuous reconstruction in a region between two cell sizes.

Similar triangulations can be found for nearly any type of mesh topology, but to limit the number of patterns to a countable level, we prohibit cell level changes greater than one in neighboring cells during the initial database setup. Thus the ratio of face length in two adjacent cells will be either one or two. This limitation, which is also commonly used in tree-based adaptive grid methods,^{16,17} reduces the number of patterns to six: cells with four undivided faces, cells with one divided and three undivided faces; cells with two

adjacent faces divided; cells with two opposite faces divided; cells with three faces divided; and cells with all four faces divided. These six patterns are shown in Fig. 7 along with appropriate triangulations. Because only six patterns must be recognized, the logic for the triangulation is straightforward and the overhead for locating the triangles within a given square is small so that the search advantage of the Cartesian mesh is not lost. The reconstruction process applies equally to any triangle whether it is a portion of a regular region of the mesh or one with unequal sides. Consequently, the modified triangulation adds no complexity to the reconstruction procedure and allows the overall structure of the Cartesian grid to be retained.

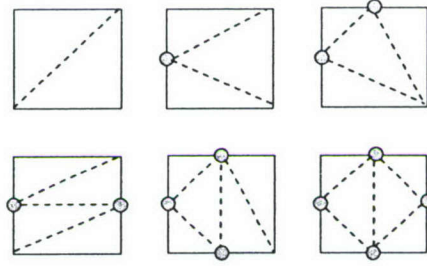


Figure 7. Six possible cell refinement patterns indicating acceptable triangulation patterns for each.

Storage and Timing Comparisons Next we present some timing comparisons for the adaptive reconstruction procedure and some representative reconstruction results. We consider properties evaluations for three fluids, CO_2 , H_2O and air. Statistically significant information for timing is obtained by considering several different zones in the p - T domain for each fluid. Some of the reconstruction regions include the discontinuity across the liquid-vapor line while some are restricted to continuous property regions. For these two-phase regions, we also compare thermodynamic procedures that treat the two phases as a single fluid with procedures that treat them as two distinct fluids. Following the definition of these various zones, we show the tree-structure grid for reconstruction to both 1% and 0.1% accuracy. Finally we compare the time required for the table look-up procedure and the complete REFPROP solution.

Figure 8 shows the density of CO_2 as a function of pressure and temperature as obtained from REFPROP. The liquid-vapor line is shown along with the global density variation. Four different rectangular zones are used for reconstruction databases. Zone 1 comprises the temperature and pressure ranges, $500\text{K} \leq T \leq 1600\text{K}$, $0.01\text{MPa} \leq p \leq 1000\text{MPa}$ and lies entirely within the vapor region. The grid structures for this zone are shown on Fig. 9 for accuracies of 1% and 0.1%. The grid color is keyed to the magnitude of the density. The 1% accuracy case requires a total of ten levels of refinement and results in 22,000 reconstruction points. The 0.1% case requires 11 refinement levels and 225,000 points. Similar results are obtained for Zones 2 and 3. The table fit and reconstruction are done on the basis of the logarithm of the pressure. The size of the reconstruction maps is summarized in Table I.

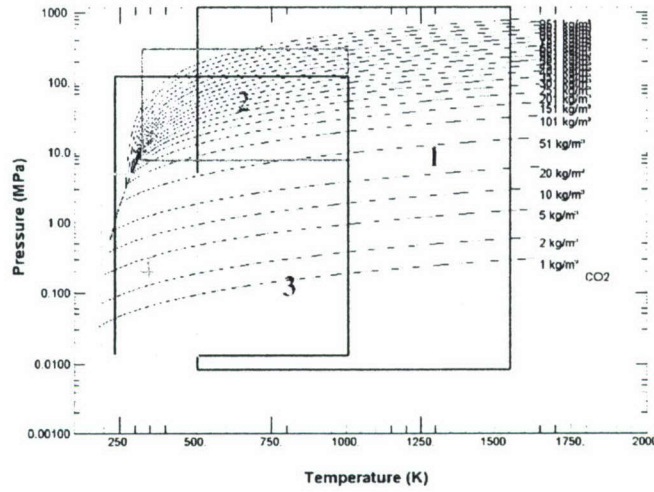


Figure 8. Density of CO_2 as a function of pressure and temperature (from REFPROP). Reconstruction databases have been obtained for four zones: Zones 1 and 2 do not include the vapor-liquid line: Zones 3 and 4 overlap the discontinuity.

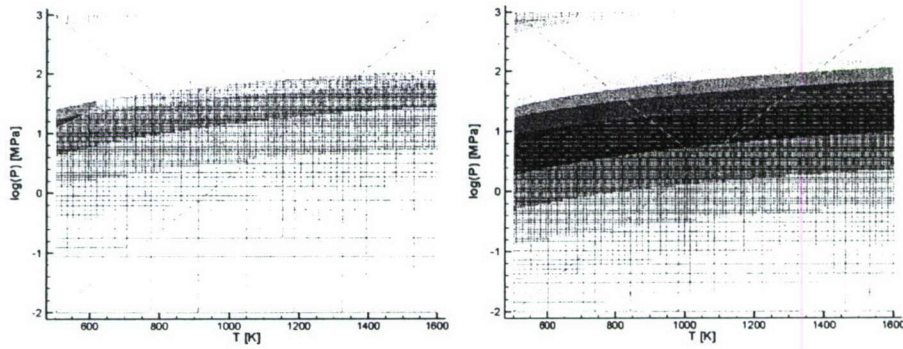


Figure 9. Adaptive reconstruction maps for Zone 1 of CO_2 (see Fig. 10). Left: 1% accuracy, 22,000 points; Right: 0.1% accuracy, 225,000 points. Timing evaluations made by performing

Zones 3 and 4 of the CO_2 map cross the liquid vapor line where the density is discontinuous. Maps with accuracies of 1% and 0.1% are shown on Fig. 10. The presence of the discontinuity implies that the refinement criterion can never be satisfied at the liquid-vapor line. We have arbitrarily terminated the refinement process for this case

at 15 levels. This implies that the errors will be less than the stated values at all locations except those immediately adjacent to the liquid-vapor line.

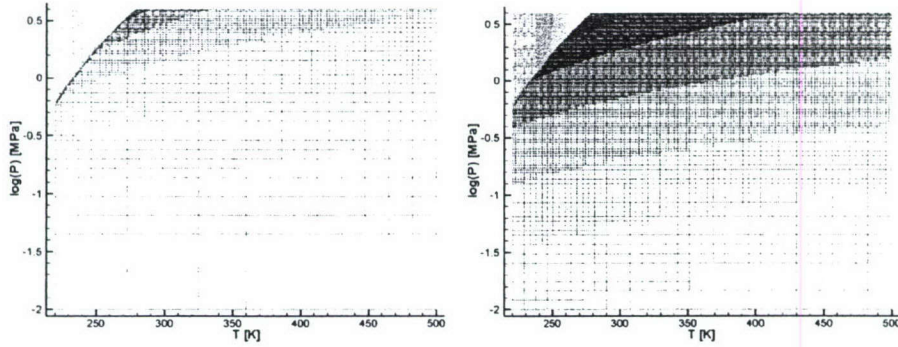


Figure 10. Adaptive reconstruction maps for Zone 4 (Fig. 10) of CO₂. Left: 1% accuracy, 72,703 points; Right: 0.1% accuracy, 108,384 points. Domain location: $220K \leq T \leq 500K$;

An alternative reconstruction map for the CO₂, Zone 4 domain, is given in Fig. 11 but with the vapor and liquid regions broken into two separate curve fits. Because it is no longer necessary to attempt to interpolate across the discontinuity, the number of reconstruction cells for a given accuracy is reduced dramatically. At the 1% accuracy level, the number of cells reduces from 22,000 for the continuous fit across the discontinuity to 5336 points in the vapor and 225 points in the liquid. Thus a total of 5561 points (and only ten levels of refinement) give the same (or slightly improved) accuracy in the ‘two-phase’ description as in the ‘single-phase’ description. For the 0.1% accuracy map, the number of reconstruction cells is reduced from 108,000 to 52,296 in the vapor plus 1102 points in the liquid region.

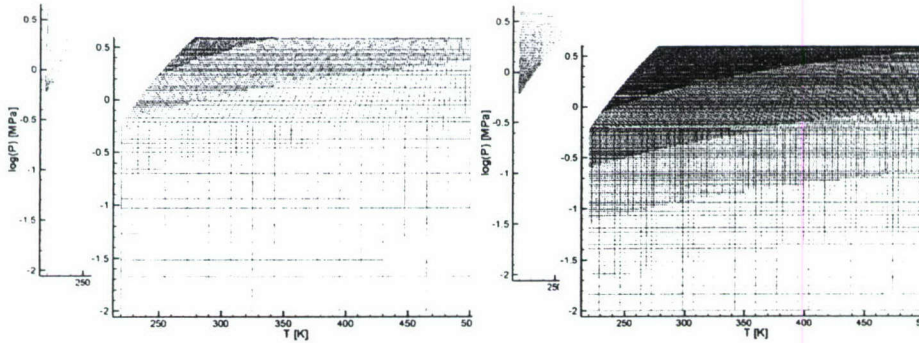


Figure 11. Adaptive interpolation maps for Zone 4 of CO₂ (see Fig. 10). Left: 1% accuracy, 225 points in liquid zone, 5336 points in vapor zone; Right: 0.1% accuracy, 1102 points in liquid zone,

Similar properties databases have been generated for water and air. The density contour maps for these two fluids are shown in Figs. 12 and 13 along with two zones for which properties data have been generated in a manner similar to that discussed above for CO₂. For brevity, the Cartesian maps for these cases are not given here, but the resulting table sizes and the reconstruction times are included in Table I discussed below.

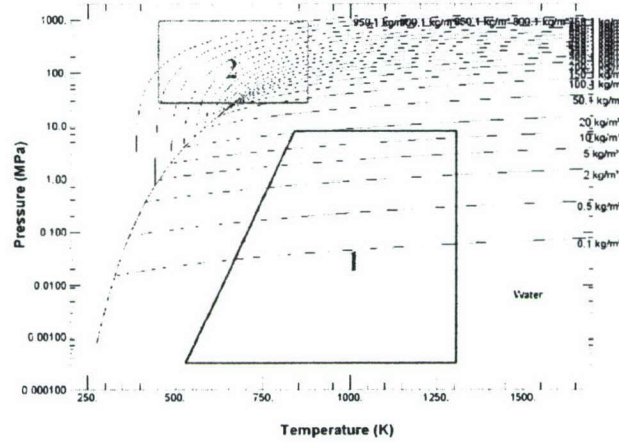


Figure 12. Density of H₂O as a function of pressure and temperature (taken from REFPROP). Interpolation databases

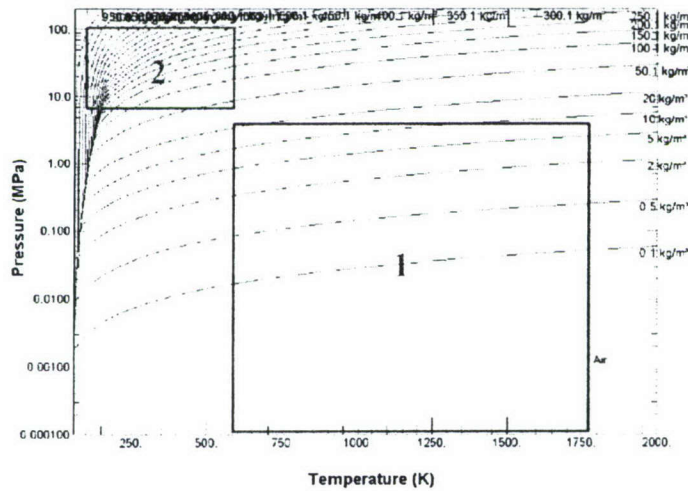


Figure 13. Density of Air as a function of pressure and temperature (taken from REFPROP). Interpolation databases have been obtained for the two zones indicated.

CPU Comparisons with C^0 Reconstruction Method. An assessment of the property evaluation times required for the adaptive reconstruction procedure as compared to that for the original REFPROP routine is given in the bar chart on Fig. 14. Timing comparisons are shown for four zones of carbon dioxide, two zones of water and two zones of air. The evaluation times are plotted on a logarithmic scale with three bars given for each fluid zone. The bars represent, respectively, the time for reconstruction accuracies of 1% and 0.1% along with the time for the REFPROP evaluations. All timings are based on making 100,000 property evaluations at equally spaced points on diagonal lines across the respective fluid zones (as indicated by the dashed lines on Fig. 9 for CO_2). The reconstruction timings are for the C^0 method. The added cost for the C^1 and C^2 methods is indicated later.

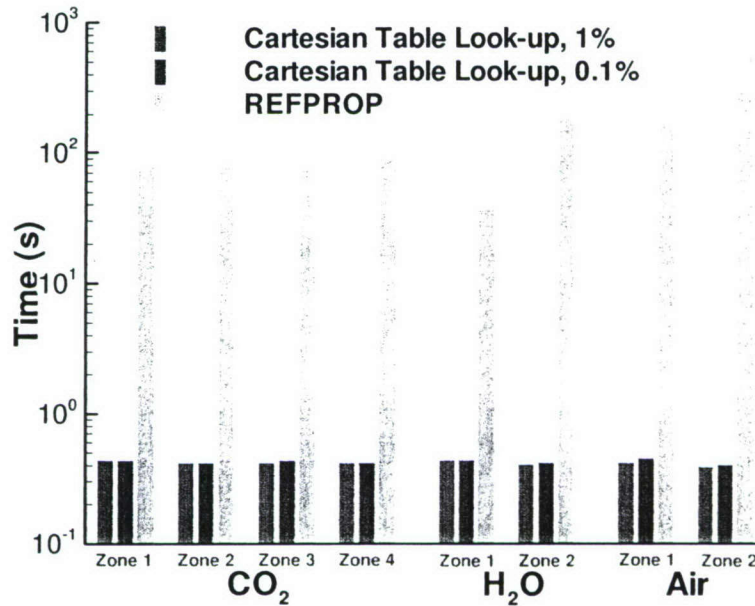


Figure 14. Comparison of CPU time of adaptive Cartesian property reconstruction and REFPROP calculation.

The timing evaluations in Fig. 14 immediately show the advantage of the reconstruction procedure. In all cases, reconstruction is at least two orders of magnitude faster than the complete REFPROP routines. The evaluation times for reconstruction are essentially the same for all fluid types, all fluid regions, and for the two accuracy levels. This insensitivity of evaluation time to accuracy level (table size) is a clear indication of the effectiveness of the tree structure in the reconstruction table. By contrast, the evaluation times for the REFPROP routines vary considerably with fluid type and fluid region because the complexity of the underlying equations changes. Air, which is treated as a mixture, is considerably more expensive to evaluate than the pure fluids. Because of the timing variability in REFPROP, the smallest time ratio occurs in Zone 1 for H_2O where reconstruction is 85 times faster while the maximum advantage occurs for air where

reconstruction is as much as 2500 times faster. The savings achieved by the reconstruction procedure would clearly be smaller for equations of state based upon simpler algebraic equations, but even for the simplest equations, the procedure remains competitive.

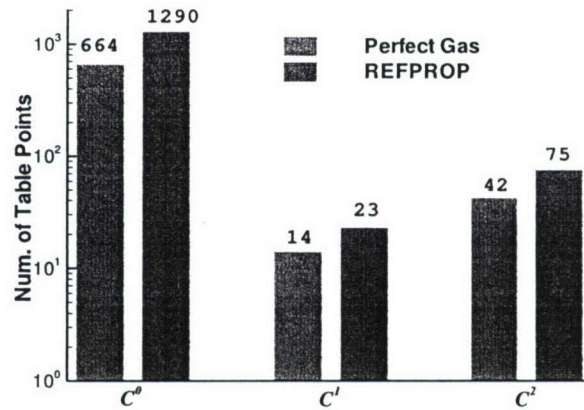


Figure 15. Storage Comparison of different reconstruction methods. CO_2 , 1% accuracy. Domain location: $500K \leq T \leq 1000K$; $1MPa \leq p \leq 100MPa$.

The timing results in Fig. 14 are also tabulated in Table I along with the number of refinement levels and the total number of cells in each zone. The times required for making the 100,000 property evaluations are also given for an equally spaced table to indicate the penalty incurred by the tree-structure. The cost of a tree-based reconstruction is approximately 12% larger than that for the equally spaced database. The overhead arises mainly from the coordinate transformation and local triangle selection within a square. A numerical value of the ratio of the adaptive reconstruction time to the REFPROP evaluation time is also included. The columns in Table I are defined in Table II.

One caution in interpreting these comparisons is that REFPROP uses the Helmholtz function which expresses fluid properties as functions of temperature and density as the fundamental thermodynamic variable. Property evaluations in REFPROP based upon pressure and temperature will therefore incur some penalty. To demonstrate that this is not the major reason for the advantage of the adaptive method, the CO_2 properties evaluation in Zone 2 was chosen as a representative comparison. The time required for 100,000 property evaluations at equally spaced points based upon pressure and temperature was 76.5 s as noted in Table I. Similar evaluations, based upon density and temperature required 45.1 s, a savings of 42 percent over the pressure and temperature pair. Therefore for CFD codes that are based upon density and temperature, the CPU advantages of the adaptive Cartesian method would be reduced by approximately a factor of two, still providing a major savings. For codes based upon other variables pairs, the speed-ups in Table I remain appropriate.

Table I. Storage and Timing Comparisons for Properties Evaluation

Fluid	Zone	Max Err	No. Levels	No. Points	Time(s) Cartes	Time(s) E.E.M [#]	Time(s) REFPROP	Time Ratio
CO ₂	1	1%	10	22,246	0.438	0.375	77.686	177.4
		0.1%	11	225,121	0.438	0.375	77.297	176.5
	2	1%	17	25,990	0.422	0.375	76.532	181.4
		0.1%	20	25,7841	0.422	0.375	76.250	180.7
	3	1%	15 [*]	15,9325	0.422	0.375	73.022	173.1
		0.1%	15 [*]	80,1151	0.438	0.375	73.250	167.2
	4	1%	15 [*]	72,703	0.422	0.375	87.329	207.1
		0.1%	15 [*]	108,384	0.422	0.375	87.563	207.5
	4	1%	5	86				
	(Liquid)	0.1%	7	1102				
	4	1%	10	5336				
	(Vapor)	0.1%	12	52,296				
H ₂ O	1	1%	10	28,391	0.438	0.375	36.234	82.7
		0.1%	12	225,121	0.438	0.375	36.343	83.0
	2	1%	9	871	0.406	0.375	186.107	458.4
		0.1%	11	8049	0.422	0.375	186.796	442.6
Air	1	1%	11	63,740	0.422	0.375	202.672	480.3
		0.1%	12	79,3657	0.453	0.375	202.203	446.4
	2	1%	8	459	0.391	0.375	989.203	2530.0
		0.1%	10	4184	0.406	0.375	989.532	2437.3

*: The lowest level allowed (for cases where discontinuity presents)

[#]: Equivalent Equal-sized Mesh (A uniform mesh refined to the deepest level)

Table II Column Information in Table I

Column	Heading	Information
1	Fluid	Fluid Type
2	Zone	Zone
3	Max Err	Maximum error of curve fit
4	No. Levels	Number of refinement levels needed (or allowed in cases with property discontinuity)
5	No. Points	Number of points in the adaptive database
6	Cartes Time	Time required for 100,000 property evaluations using adaptive database
7	Time(s) E.E.M.	Time required for 100,000 property evaluations using equally spaced database.
8	REFPROP Time	Time required for 100,000 property evaluations using REFPROP
9	Time Ratio	Ratio of REFPROP to adaptive database property evaluation time

Table Size Comparison of C^0 , C^1 and C^2 Reconstruction Methods. The above results have shown the CPU time advantages of the adaptive reconstruction method. In the present subsection, we compare the table sizes required for the C^0 , C^1 and C^2 reconstruction procedures. The comparisons are obtained for the rectangular temperature-pressure region, $500K \leq T \leq 1000K$, $1MPa \leq p \leq 100MPa$, in CO_2 using an error tolerance of 1%. In the lower pressure portion of this region, CO_2 behaves as a perfect gas, while in the upper regimes it is strongly supercritical (see Fig. 8). The sizes of the storage tables for the three interpolation levels are given in Fig. 15. In computing these tables, the Gibbs function and its first two derivatives were obtained from analytical expressions within REFPROP but the high order derivatives (greater than two) were obtained by numerical differentiation. The number of cells required for the C^0 reconstruction method was 1290, while the C^1 method decreased the table size to only 23 cells. The C^2 reconstruction, however, required 75 cells to achieve the same accuracy, suggesting a sensitivity in the C^2 reconstruction procedure to the high order derivatives. This phenomenon may arise from two issues. First, the Gibbs function, rather than the density and enthalpy themselves, is fitted in the C^2 reconstruction and the density and enthalpy are obtained by differentiating the Gibbs function. Second, the C^2 reconstruction uses higher order polynomials that are more prone to oscillate and this tendency may require increased resolution to realize a given accuracy.

To demonstrate that this trend in the storage size is not related to the method in which the REFPROP evaluation are made, we have added in Fig. 15 companion reconstruction results for a perfect gas using the same pressure-temperature region in CO_2 . Here, all partial derivatives were computed analytically and the specific heats were taken as

constant. The perfect gas tables for C^0 , C^1 and C^2 reconstruction have 664, 14 and 42 mesh points respectively, again indicating a significant savings in moving from C^0 reconstruction to its C^1 counterpart with a modest increase for C^2 reconstruction.

Sample CFD Calculations

In the present section we present some representative computational results to demonstrate the method. We begin with a one-dimensional computation that is used to verify the method and to provide timings. We then present a two-dimensional example that demonstrates some of the thermodynamic characteristics that are enabled by the present formulation. These computations are based on the results of an in-house CFD code. The code uses a second-order accurate, approximate Riemann solver in space with a two equation turbulence model. The focus in these examples is on demonstrating the efficiency and practicality of real fluid computations.

One-Dimensional Flow Computation. As an initial example of the timing realized with the adaptive reconstruction method, we use a simple one-dimensional example of subsonic flow through a convergent-divergent nozzle. The nozzle is symmetric about the throat with the inlet and exit areas 1.25 times the throat area. The working fluid is chosen as water with an inlet total pressure of 60 MPa and stagnation temperature of 750 K. The back pressure at the outlet is 50 MPa. These parameters place the solution in Zone 2 of the H₂O property map on Fig. 14. A total of 200 cells are used in the calculation. The convergence rates for this case using the C^0 , C^1 and C^2 methods were originally shown in Fig. 7 where we noted that the convergence with all three of these reconstruction methods was identical to the convergence obtained by coupling the REFPROP routines directly into the CFD code, so long as the triangulation depicted in Fig. 8 is used. Correspondingly we showed that convergence on the triangulation of Fig. 2 stalled. Although the number of iterations is essentially identical for the different property evaluation methods, their CPU costs are significantly different.

Figure 16 shows the cumulative CPU time required for the computation as a function of iteration number for 1000 iterations. The C^0 reconstruction method results in the fastest execution. Comparison of the results for the inconsistent and the consistent triangulation methods indicates that the subdivided triangular mesh increases the CPU time by about 5% as compared to the diagonally divided triangles, indicating a minor overhead for locating a particular triangle inside each square. The costs of the C^1 and C^2 methods are nearly equal and are approximately twice that of the C^0 method. The C^2 method evaluates all properties from a single ninth-order polynomial from while the C^1 method evaluates properties from separate fifth-order polynomials for density and enthalpy. The calculation based on the exact property evaluation from REFPROP is approximately 160 times slower than the C^0 method and 80 times slower than the C^1 and C^2 methods, again in keeping with the timing of the properties evaluation themselves.

The CPU time for a CFD calculation can be broken into two parts: the property evaluation time and the equation solution time. The relative advantages of faster property evaluation times clearly will decrease as the complexity of the equation solution increases, and in particular as we move from one to three dimensions. The nominal cost

of the property evaluation by REFPROP in this region of the H_2O map is about 450 times that of the C^0 integration method (see Table I). For this one-dimensional case, the CFD calculation time ratio is 160, suggesting that the equation solution time is roughly 80 percent longer than the C^0 interpolation time in the CFD calculation. Experiments on a PC show that the one-dimensional solver costs about $61.25 \mu s / (cell \times iteration)$, and our in-house 2D and 3D unstructured codes cost about $100.2 \mu s / (cell \times iteration)$ and $200.9 \mu s / (cell \times iteration)$ respectively. Assuming the property evaluation time does not change when going from 1D to 2D and 3D calculations, this indicates that the 2D calculation with the C^0 interpolation method will be 115 times faster than the direct REFPROP evaluation calculation and the 3D calculation will be 66 times faster.

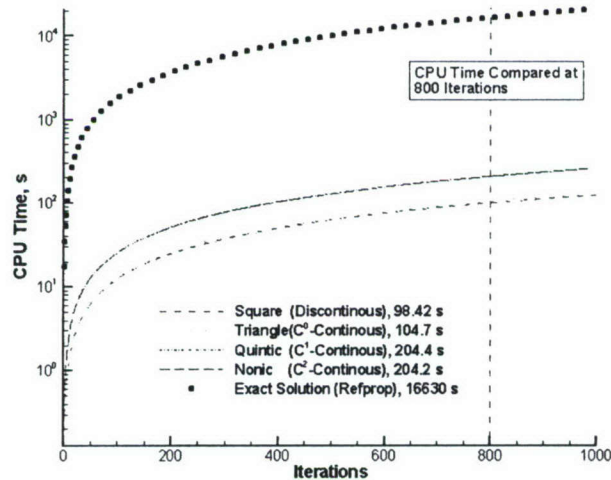


Figure 16. CPU time comparison for different interpolation methods

The CPU time for a CFD calculation can be broken into two parts: the property evaluation time and the equation solution time. The relative advantages of faster property evaluation times clearly will decrease as the complexity of the equation solution increases, and in particular as we move from one to three dimensions. The nominal cost of the property evaluation by REFPROP in this region of the H_2O map is about 450 times that of the C^0 integration method (see Table I). For this one-dimensional case, the CFD calculation time ratio is 160, suggesting that the ratio of equation solution time to property evaluation time in a one-dimensional calculation is approximately 1.8. Numerical computations show that the one-dimensional solver requires about $61.25 \mu s / (cell \times iteration)$. Corresponding costs for two- and three-dimensional solutions are 100.2 and $200.9 \mu s / (cell \times iteration)$ respectively. Assuming the property evaluation time does not change when going from one to three dimensions, this suggests that a two-dimensional calculation with C^0 interpolation method will be 115 times faster than the direct REFPROP evaluation calculation and the three-dimensional calculation will be 66 times faster. Solutions based upon C^1 and C^2 reconstruction will be about half this amount.

Two-Dimensional Real-Fluid Example. The geometrical configuration for the 2-D computation is again a C-D nozzle patterned after one designed for hypersonic flow testing at ultra high pressures.²⁸ The working fluid is air with upstream stagnation conditions of 1700 MPa and 750 K. The density of air at these conditions is approximately equal to that of water and the resulting acceleration through the choked throat shows dramatic real-fluid characteristics. The convergent section of the nozzle is very strongly converging and the inflow starts at low speeds.

We limit our results here to a Mollier chart for air showing the physical regime of interest and comparisons between solutions of the real-fluid and corresponding perfect gas computations at the same pressure and temperature. The Mollier diagram is shown on the left half of Fig. 17 along with the h - s domain covered by the flow in the nozzle. Specifically, the enthalpy and entropy values in all cells in the computational domain are plotted on the h - s diagram superimposed upon the thermal database from REFPROP. The solution forms a roughly triangular region. The left edge of this triangular region corresponds to the thermodynamic path of the fluid on the centerline. As can be seen, the fluid on the centerline undergoes an approximately constant entropy process. The upper edge of the triangle corresponds to the fluid adjacent to the wall and shows its entropy continues to increase while the enthalpy decreases slightly in agreement with classical results for the adiabatic recovery temperature on a nozzle wall. The horizontal constant pressure lines to the right side of the Mollier diagram correspond to the perfect gas region where enthalpy is independent of pressure. The nearly vertical constant pressure lines on the left side indicate a strong real-fluid effect of pressure on enthalpy. These lead to a very different temperature pattern in the nozzle as the contours in the right half of Fig. 17 show.

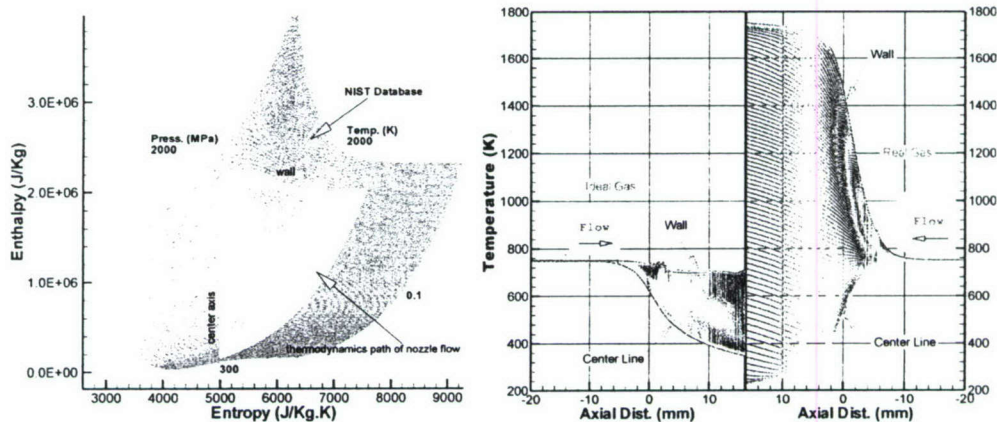


Figure 17. 2D calculation of ultra-high pressure flow through hypersonic nozzle. Left: Mollier diagram and h - s domain of solution; Right: Temperature along the nozzle for calculation with real fluid properties and perfect

The temperature distribution in the nozzle for a perfect gas calculation is compared with that for the real-fluid calculation on the right half of Fig. 17. Here, the temperature in

every computational cell has been plotted at its appropriate axial location in the nozzle. The left side of the plot shows the temperature for the perfect gas solution with the axial coordinate running from left to right. The right side of the plot shows the results for the real-fluid case with the axial coordinate running from right to left. There is clearly a major difference between the two solutions. In both solutions, the upper bound on the temperature at any axial location corresponds to the wall, while the minimum temperature represents the value in the free stream. For the perfect gas, the temperature on the wall (the upper bound) decreases slightly from its upstream value of 750 K, while for the real fluid, the wall temperature rises rapidly throughout, reaching over 1400 K at the throat ($x = 0$) and continuing to above 1800 K. Contrasting the increased wall temperature with the nearly constant stagnation enthalpy for the real fluid calculation in the Mollier diagram on the left plot of Fig. 17 demonstrates that the wall enthalpy for the real fluid behaves like that for the perfect gas in that it remains essentially constant throughout the nozzle. The wall temperature for the real-fluid solution, however, increases rapidly because of the strong, real-fluid, pressure dependence of enthalpy. The minimum temperature at any axial location is also lower for the real fluid than for the perfect gas, again indicating how much the real-fluid thermodynamics differ from the perfect gas assumption. As a final point, we note that both the convergence rates and the CPU times for the perfect gas and real fluid computations were nearly identical, thus verifying that the reconstruction procedure provides an effective thermodynamic interface for real-fluid computations.

Hybrid RANS/LES Modeling in High Pressure Fluids

Contemporary turbulence modeling efforts emphasize large eddy simulations (LES) and, more recently, hybrid RANS/LES models, but efforts in these areas have been largely limited to incompressible fluids and perfect gases. Application of these methods to arbitrary fluids requires careful adaptation to ensure that the thermodynamics, the numerics and fluid dynamics are properly coordinated to give accurate and efficient results. Our focus here is on developing methods that can be applied to practical T&E applications to take into account flow fields that contain both traditional high Reynolds number boundary layers and regions with large scale unsteadiness that is not accurately resolved by unsteady RANS methods. For this reason, our focus is on hybrid RANS/LES models that are compatible with traditional second-order CFD algorithms.

To adapt the generalized fluid dynamic formulation outlined above to hybrid RANS/LES modeling, it is necessary to reduce the level of artificial dissipation in the algorithm. The numerical dissipation in characteristics-based, upwind methods is determined by the eigenvalues of the problem and the time-marching derivative. The artificial pseudo-time coefficient matrix offers flexibility for controlling this dissipation. The flux formulation for a general upwind finite volume approach can be interpreted as the average of the fluxes on either side of the cell interfaces augmented by an artificial dissipation term, $\tilde{E} = \{E_L + E_R\} - \Gamma |\Gamma^{-1} A_p| (Q_{pR} - Q_{pL}) / 2$. Clearly, the magnitude of the artificial dissipation is proportional to the coefficient matrix, Γ . The key requirements on this term are that it provide sufficient dissipation to prevent solution instability and that it

scale properly at various flow limits including low speeds, low Reynolds numbers and high Strouhal numbers. To reduce the artificial dissipation, we introduce a modified dissipation matrix that improves accuracy while maintaining convergence, so that the numerical flux becomes, $\tilde{E} = \frac{1}{2}(E_L + E_R) - \frac{\alpha}{2}\Gamma[D](Q_{pR} - Q_{pL})$ where D is a diagonal matrix in which one entry corresponds to the largest pseudo-acoustic value and the remainder are the particle speed, while α is a parameter to be adjusted. Analytical and numerical experiments suggest that the scheme is unstable for $\alpha \geq 1$ and becomes stiff as $\alpha \rightarrow 0$. The value $\alpha = 0.5$ represents a compromise between stability and accuracy and is used in the calculations below.

The modified artificial dissipation is first verified by comparing with the analytical solution for an infinite array of counter-rotating vortices whose amplitudes decay with time. The results on the left of Fig. 18 for inviscid flow and $Re = 100$ were computed with $CFL_u = 0.1$. The standard ('non-preconditioned') calculation shows that both cases decay rapidly demonstrating the accepted observation that unmodified upwind schemes are unacceptable for DES applications. When 'characteristic dissipation' is used, the inviscid case decays by about 1% in two non-dimensional time units, while the $Re = 100$ case decays by 4.7%. Although this is a major improvement, the decay rates are still too fast. With the modified dissipation, the inviscid case decays by approximately 0.04% in two non-dimensional time units while the $Re = 100$ case decays approximately 3.7%, slightly slower than the exact solution. Accurate calculations require that both the CFL and the VNN numbers be controlled and this small error becomes larger as Re is reduced. To demonstrate accuracy at lower Re numbers we show on the right side of Fig. 18 results for a CFL of 0.0036 for Reynolds numbers of infinity, 100, 10 and 1. At $Re = 1$, $CFL = 0.0036$ corresponds to $VNN = 0.36$, while at $CFL = 0.1$ and $Re = 100$ the von Neumann number is 0.1. The results at this viscous-controlled time step indicate the modified dissipation continues to provide accuracy at all Reynolds numbers. Overall, the results of the Taylor vortex problem suggest the modified dissipation provides a reasonable solution for large-scale motions.

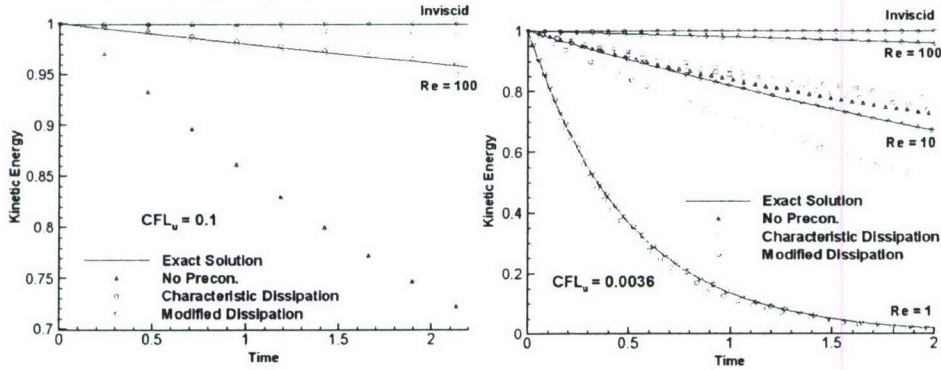


Figure 18. Rate of decay of kinetic energy at different Reynolds numbers for Taylor vortices problem. Left: $CFL_u = 0.1$; Right: $CFL_u = 0.0036$. Comparison with analytical solution.

The scaling constant, C_{DES} , in the DES implementation was calibrated by comparing results against the decay of homogeneous turbulence downstream of a grid as reported by Comte-Bellot and Corrsin. Figure 19 shows the energy spectra for calculations using the characteristic and modified dissipation terms along with the experimental results and a line showing the $E(\kappa) \sim \kappa^{-5/3}$ slope. The value of the DES coefficient, C_{DES} , in these cases is 0.78. It can be clearly seen that the modified dissipation significantly improves the simulation. When C_{DES} is calibrated against experiment (the right side of Fig. 19) the turbulence decay is commensurate with the experiment. In Fig. 19 C_{DES} of 0.5 appears to give the best agreement with experiment and is adopted in the solutions given below.

Representative DES solutions are compared with unsteady RANS calculations in Fig. 420 for a shear layer representing the mixing between air and nitrogen at high pressures. The results indicate substantially better resolution for the modified scheme. Efforts are present are aimed at extending these results to larger grid aspect ratio cases (above 100) to enable extensions to higher Reynolds numbers.

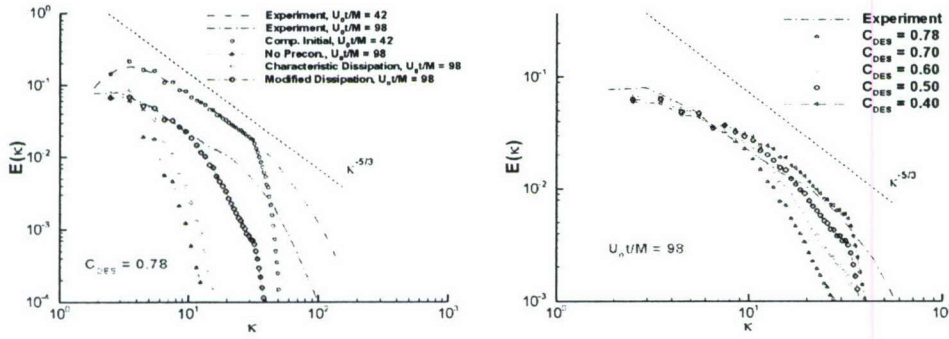


Figure 19. Energy spectra in decaying homogeneous turbulence for different preconditioning methods (left) and for different C_{DES} values (right).

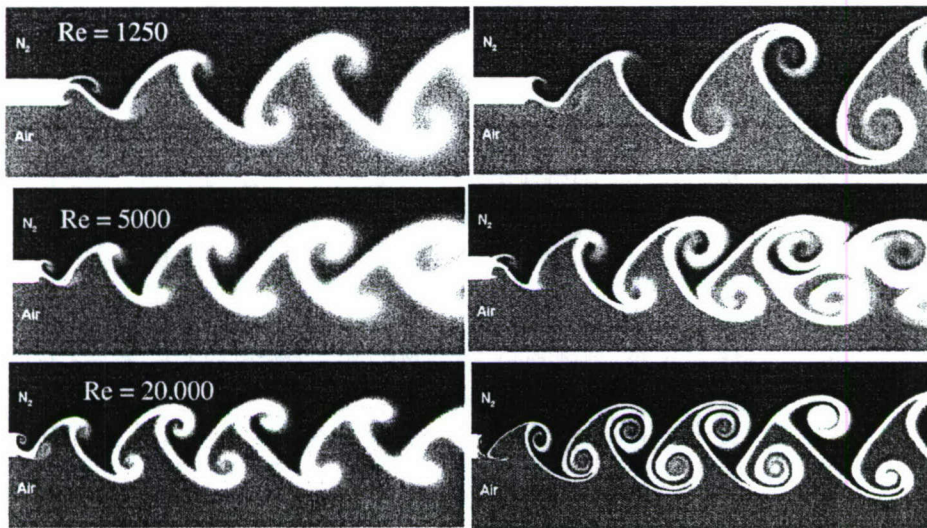


Figure 20. Comparison of RANS (left) and DES (right) calculations for shear layer mixing in high pressure flow.

References

1. Lemmon, E.W., Jacobsen, R.T., Penoncello, S.G., and Friend, D.G., "Thermodynamic Properties of Air and Mixtures of Nitrogen, Argon and Oxygen from 60 to 2000 K at Pressures to 2000 Mpa," *J. Phys. Chem. Ref. Data*, Vol 29, No. 3, p 331-385.
2. Lemmon, E.W., "Ultra High Pressure Air Properties and CFD Code," Presentation at AFOSR Test and Evaluation Portfolio Review, August 15-16, 2006, Washington, D.C.
3. K. Parke and W. G. Klottingham, On the Problem of Crack Extension in Brittle Solids under General Loading. Report SM 74-8, Graduate Aeronautical Laboratories, California Institute of Technology, Pasadena, 1974.

Personnel Supported During Duration of Grant

Guoping Xia	Postdoc, Purdue University
Hogirl Jung	Ph.D. Student, Purdue University

Publications

"Consistent Properties Reconstruction on Adaptive Cartesian Meshes for Complex Fluids Computations," Xia, G., Li, D. and Merkle, C.L., *J.Comp. Physics*, Vol. 225, No. 1, 2007.

"A Hyperbolic Algorithm for Numerical Solutions of Coupled Plasma/EM Fields Including Both Real and Displacement Currents," Li, D., Merkle, C.L., Scott, M., Keefer, D., Moeller, T., and Rhodes, R., 'AIAA-2007-5745, 43nd AIAA/ASME/SAE/ASEE Joint Propulsion Conference and Exhibit, Cincinnati, OH, July 8-11, 2007.

"Detailed Flowfield Predictions of Heat Transfer to Supercritical Fluids in High Aspect Ratio Cooling Channels," Jung, H., Merkle, C.L., Schuff, R. and Anderson, W. A., 'AIAA-2007-5548, 43nd AIAA/ASME/SAE/ASEE Joint Propulsion Conference and Exhibit, Cincinnati, OH, July 8-11, 2007.

"Cartesian Adaptive Properties Interpolation for Computations of Complex Fluids," G. Xia, D. Li, C. Merkle, AIAA-2006-1293, 44th AIAA Aerospace Sciences Meeting and Exhibit, Reno NV, Jan . 9-12, 2006.

"Modeling of Turbulent Mixing Layer Dynamics with Finite Splitter Plate Thickness and Real Fluid Effects," G. Xia, D. Li, V. Sankaran, C. Merkle, AIAA-2006-3729, 36th AIAA Fluid Dynamics Conference and Exhibit, San Francisco CA, June 5-8, 2006.

"Multi-Disciplinary Computational Analysis in Propulsion," C. Merkle, D. Li and V. Sankaran, AIAA-2006-4374, 42nd AIAA/ASME/SAE/ASEE Joint Propulsion Conference, Sacramento, CA, July 10-12, 2006.

Honors & Awards Received

ASME Fellow—awarded January 1995.

Reilly Professor of Engineering, Purdue University, Aug. 2003-present.

H.H. Arnold Chair of Computational Mechanics, University of Tennessee, August 1996-August 2003.

AFRL Point of Contact

John Felderman, AEDC, Tullahoma, TN, Phone 931-454-5640. Met at Purdue October 14, 2005 and at AIAA meeting, June 6, 2006.

Transitions

The GEMS computer code has been delivered to AEDC for analysis of multi-phase fluid dynamics in test facility analysis. Point of contact at AEDC (ATA) is Michael Scott, AEDC, Tullahoma TN, Phone: 931-454-3321.

New Discoveries

None